Bioactive Materials 13 (2022) 239–248

Contents lists available at ScienceDirect

Bioactive Materials

journal homepage: www.keaipublishing.com/en/journals/bioactive-materials

Picomolar-sensitive β-amyloid fibril fluorophores by tailoring the hydrophobicity of biannulated π-elongated dioxaborine-dyes

Jusung An [a,1], Peter Verwilst [b,1], Hira Aziz [c,d,1], Jinwoo Shin [a,1], Sungsu Lim [c], Ilwha Kim [a], Yun Kyung Kim [c,d,**], Jong Seung Kim [a,*]

[a] Department of Chemistry, Korea University, Seoul, 02841, South Korea
[b] KU Leuven, Rega Institute for Medical Research, Medicinal Chemistry, 3000, Leuven, Belgium
[c] Convergence Research Center for Diagnosis, Treatment and Care System of Dementia, Brain Science Institute, Korea Institute of Science and Technology (KIST), Seoul, 02792, South Korea
[d] Division of Bio-Medical Science & Technology, KIST School, Korea University of Science and Technology (UST), Seoul, 02792, South Korea

ARTICLE INFO

Keywords:
β-Amyloid
Small-molecular fluorescent probe
Dioxaborine-dye
Hydrophobicity tailoring
Alzheimer's disease

ABSTRACT

The pathological origin of Alzheimer's disease (AD) is still shrouded in mystery, despite intensive worldwide research efforts. The selective visualization of β-amyloid (Aβ), the most abundant proteinaceous deposit in AD, is pivotal to reveal AD pathology. To date, several small-molecule fluorophores for Aβ species have been developed, with increasing binding affinities. In the current work, two organic small-molecule dioxaborine-derived fluorophores were rationally designed through tailoring the hydrophobicity with the aim to enhance the binding affinity for $A\beta_{1\text{-}42}$ fibrils —while concurrently preventing poor aqueous solubility—*via* biannulate donor motifs in D-π-A dyes. An unprecedented sub-nanomolar affinity was found ($K_d = 0.62 \pm 0.33$ nM) and applied to super-sensitive and red-emissive fluorescent staining of amyloid plaques in cortical brain tissue *ex vivo*. These fluorophores expand the dioxaborine-curcumin-based family of Aβ-sensitive fluorophores with a promising new imaging agent.

1. Introduction

Aberrant deposits of amyloid beta (Aβ) peptides are a major pathological hallmark in Alzheimer's disease (AD) [1,2]. Aβ pathology first starts to occur in the asymptomatic stage of AD onset, and the extracellular Aβ accumulation in matured Aβ aggregates, known as amyloid plaques (or senile plaques), is primarily observed in the frontal and temporal lobes. This pathology gradually progresses to affect several regions of the neocortex, hippocampus, as well as cerebrovasculature [3–5]. Since AD is accompanied by a long prodromal phase of approximately 20 years; aberrant Aβ deposits can be found at least a decade before pathological symptoms, including memory loss, confusion, and cognitive decline of dementia [6,7]. Early diagnosis of AD is essential for establishing a prevention strategy [8,9]. At the same time, currently uncertainty remains with regards to treatment options and aggressive efforts are directed at finding a cure for AD [10]. Given this wide time gap between the discovery of deposited Aβ and the appearance of cognitive dysfunction, this provides a potential opportunity to diagnose and initiate treatment of AD. However, it requires an accurate and reliable visualization method. Additionally, detecting senile plaques in postmortem brain sections is an indicator of AD progression. Accurately and sensitively detecting this insoluble analyte is indispensable in histological and pathological studies of AD, thereby improving the quantification and detection of the neuropathological lesions [11]. Among the current tools to reveal AD pathology, fluorescence spectroscopy is an incomparably convenient and economical experimental technique, usually in a non-invasive manner [12]. Hence, fluorescence spectroscopy has been established as a cornerstone in basic and pre-clinical research as a fundamental tool at (sub-)cellular and small-animal scales. Above all, a high degree of sensitivity is required to enable an

Peer review under responsibility of KeAi Communications Co., Ltd.
* Corresponding author.
** Corresponding author. Convergence Research Center for Diagnosis, Treatment and Care System of Dementia, Brain Science Institute, Korea Institute of Science and Technology (KIST), Seoul, 02792, South Korea.
E-mail addresses: yunkyungkim@kist.re.kr (Y.K. Kim), jongskim@korea.ac.kr (J.S. Kim).
[1] These authors contributed equally to this work.

https://doi.org/10.1016/j.bioactmat.2021.10.047
Received 6 October 2021; Received in revised form 22 October 2021; Accepted 30 October 2021
Available online 9 November 2021

excellent performance of these fluorescent dyes toward potential targets in biological environments [13]. This sensitivity can be achieved through various means, for instance, functional selectivity where the fluorescent behavior of the fluorophore depends on environmental factors, conformational changes or *in situ* liberation of a dye, or superior binding affinity [14]. The latter has the advantage that tight and selective binding of a fluorophore would potentially enable future developments into other imaging modalities that could find clinical applications, e.g. Positron Emission Tomography (PET) probes as ^{11}C or ^{18}F-labeled agents [15,16].

Unlike enzymes or receptors with specific binding sites or reactivity, perniciously, various amyloid proteins involved in amyloidosis such as Aβ, α-synuclein, insulin, and hyperphosphorylated tau protein (p-Tau), are atypical proteins that exhibit less predictable binding modes with small-molecular ligands [17,18]. More concretely, previous studies suggested that the Aβ polypeptide is regularly ordered in a structural characteristic "cross-β-sheet" scaffold, in which adjacent chain segments are tightly folded in an anti-parallel way within the fiber lattice [19]. These β-strand segments' peptide chains run perpendicular to the long fibril, and van der Waals forces and electrostatic forces preserve its conformational stabilization in an aqueous system [20]. This fiber structure possesses approximately 25% of uninterrupted hydrophobic residues, and the compact coil structure displays metastability [6]. These characteristics could contribute to a global conformational rearrangement and intermolecular hydrophobic interaction, such as β-sheet secondary structure caused by fibrilization. Especially, $A\beta_{1\text{-}42}$ assumes a shape of a double-horseshoe-like cross-β-sheet as a separate entity with maximally buried hydrophobic side chains, in which residues 1–14 are organized and adopt a β-strand conformation [17]. Hence $A\beta_{1\text{-}42}$ aggregates much faster and dominates in the core of senile plaques [21,22]. Based on the intrinsic hydrophobicity of Aβ, the diverse small-molecule fluorescent dyes developed so far have been postulated to bind *via* hydrophobic π-π stacking interactions to these cross-β-sheets surfaces or intercalate into hydrophobic grooves and channels of Aβ aggregates [23,24]. Hydrophobic interactions arise from behavior that maximizes hydrogen bonding between water molecules and minimizes the area of contact between water and non-polar molecules [25,26]. Given the significant hydrophobicity of amyloid proteins, strong hydrophobicity of ligand molecules could effectively enhance binding affinity to cross-β-sheets or hydrophobic grooves through a hydrophobic effect in aqueous environments [27].

To date, several fluorescent dyes sensitive toward various states of Aβ aggregation have been reported to display a high binding affinity. Structural modifications, mainly π-elongation, have commonly been introduced as a critical strategy for small-molecular fluorophores to make bathochromic fluorescence emission and increase hydrophobicity in an aqueous medium [28–36]. However, the increased hydrophobicity associated with an extended π-conjugation also inevitably leads to poor aqueous solubility and increases the ligands' promiscuity with regard to other hydrophobic proteins and cellular components. Thus, the major challenge in the design of new red-emissive fluorophores with a stronger affinity for Aβ fibrils is not only to maintain adequate aqueous solubility but also specificity and sensitivity.

A wide range of dissociation constants (K_d) have been reported so far for dyes binding Aβ fibrils, ranging from the nanomolar to micromolar affinities [23,24]. Among them, dioxaborine-based curcumin structures have been incredibly successful, most notably the CRANAD series by Ran's group, and have been reported to show good binding affinities due to curcumin's intrinsic affinity of several Aβ species [37–40]. In 2009, the first reported dye of this series, CRANAD-2, demonstrated an strong affinity (K_d = 36.7 nM) for $A\beta_{1\text{-}40}$ fibrils and adequate photophysical properties (Table S1) [41]. The versatility of this fluorophore class has been demonstrated during the last decade, with recent work describing CRANAD-58, able to detect both soluble and insoluble $A\beta_{1\text{-}42}$ species *in vitro* and even *in vivo* [42]. In parallel, Liu et al. investigated a separate class of dyes, known as the DANIR series, with one of these demonstrating a K_d value of 1.9 nM, with remarkable fluorescent sensitivity [43]. To the best of our knowledge, DADNIR-2 from Cui's group showed the highest binding affinity ($K_d = 1.04 \pm 0.03$) reported for an $A\beta_{1\text{-}42}$ aggregate fluorescent probe thus far. However, its flat elongated structure and relatively high molecular weight may result in solubility issues [44].

In the current study, components of both the dioxaborine-based half-curcumin structures and the high-affinity DANIR dyes were rationally combined. These dyes were synthesized *via* a condensation reaction of a beta diketone with two *N,N*-dimethyl biannulated electron-donating groups: **BZ-OB** (benzofuran) and **NAP-OB** (naphthalene) (Fig. 1). Due to the relatively small number of carbon atoms and introduced oxygen atom into the aromatic ring of benzofuran, which induces a different hydrophobicity for the whole molecule structure, compared with naphthalene. Importantly, this particular diketone moiety was chosen as it previously demonstrated an excellent aqueous solubility for the corresponding dioxaborine-based half-curcumin structures *via* the suppression of intermolecular π-π stacking interaction by the isobutyl group's innate steric bulk [45].

2. Materials and methods

2.1. Quantum yield and determination of fluorescence emission and wavelength maxima

To avoid the inner filter effect during measurement of fluorescence emission, the spectra were recorded with the absorbance lower than 0.1 at wavelengths longer or equal to the excitation wavelength with HPLC grade solvents including 1,2-dichlorobenzene, 1-butanol, 1-propanol, 2-methoxy ethanol, acetone, acetonitrile, chloroform, diethyl ether, ethyl acetate, ethylene glycol dimethyl ether, ethanol, methanol, tetrahydrofuran, or toluene). The fluorescence quantum yields of **BZ-OB** and **NAP-OB** were measured versus 4-(dicyanomethylene)-2-methyl-6-(4-dimethylaminostyryl)-4*H*-pyran (DCM) in acetonitrile. (Φ_{Fl} = 0.43) [46], using a previously reported procedure [47].

2.2. Spectroscopy in a solvent with increasing viscosity

The emission spectra of **BZ-OB**, **NAP-OB**, and Thioflavin T (ThT) [48] (10 μM) in the various *v/v* % of ethylene glycol and glycerol (30, 50, 60, 70, and 80% of glycerol in ethylene glycol) at 25 °C were recorded. **BZ-OB** and **NAP-OB** stock solutions were prepared in dimethyl sulfoxide (DMSO), respectively, and all solutions contain a final concentration of 1% DMSO.

2.3. Solubility of BZ-OB and NAP-OB in aqueous solution

The absorbance of **BZ-OB** and **NAP-OB** was recorded at 495 and 523 nm, respectively, in phosphate buffered saline (PBS) (10 mM, pH = 7.4) containing 1% DMSO at different concentrations in the 0 − 50 μM range.

2.4. Spectroscopy in the presence of $A\beta_{1\text{-}42}$ and potential interferents (metal ions, amino acids, thiols, and albumin)

Stock solutions of **BZ-OB** and **NAP-OB** were prepared in DMSO and added to solutions of the analytes in PBS ($A\beta_{1\text{-}42}$ or bovine serum albumin (BSA)) or deionized water (DIW) (metal ions, amino acids, or thiols) to finally obtain a solution containing 1% DMSO. All emission signals were obtained after 5 min incubating at 37 °C with 300 rpm orbital shaking.

2.5. pH dependent absorbance of BZ-OB and NAP-OB

The absorbance and fluorescence spectra of **BZ-OB** (10 μM) and **NAP-OB** (10 μM) were recorded in DIW with the pH adjusted by hydrochloric acid or sodium hydroxide to the pH 2, 4, 6, 8, 10, or 12.

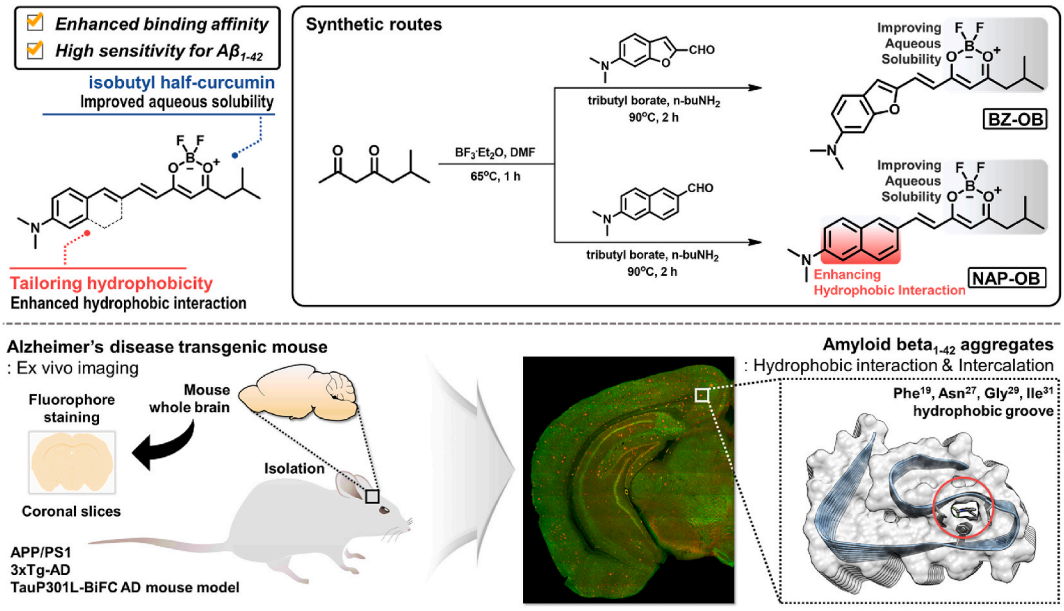

Fig. 1. Rationally designed chemical structures and brief synthetic routes of dioxaborine-based half-curcumin analogues, named **BZ-OB** and **NAP-OB**, modified with biannulated π-elongation. Illustrated overview for amyloid beta (Aβ) *ex vivo* visualization.

2.6. Photostability

A solution of **BZ-OB** or **NAP-OB** with an absorbance of 1.0 at the maximum absorbance wavelength was prepared in 1% DMSO/PBS. A 3100 K halogen lamp (Olympus LG-PS2; 12 V, 100 W) was used for irradiation, and the absorbance was recorded at 10 min intervals for 60 min.

2.7. Theoretical calculations

Density functional theory (DFT) calculations were performed using the Gaussian 16 software package [49]. The structures of **NAP-OB** and **BZ-OB** were optimized using the ωB97XD functional at the N07D level of theory, with the default IEFPCM solvation model of acetonitrile [50,51]. Molecular orbital were visualized using Gaussview 6.1 [52]. To determine the amount of intramolecular charge transfer (ICT) character upon vertical excitation to the first excited state, a calculation based on the differences in electron density was used [53], and results were analyzed using Multiwfn 3.8 [54]. For these calculations, the molecular structure was recalculated at the CAM-B3LYP/N07D level of theory [55], using the IEFPCM model of water and time-dependent density functional theory (TDDFT) vertical excitations were performed using the same solvation model and the optimized structure of the ground state.

2.8. Docking studies

The ground-state B3LYP-optimized structures of **BZ-OB** and **NAP-OB** were used as the ligands for docking studies. The cryogenic electron microscopy (cryo-EM) structure of $A\beta_{1-42}$ (PDB ID: 5OQV) [56] was prepared by removing either the Glu^{22} or Val^{18} -facing conformation of Phe^{20}, and one entire protofibril was encompassed within the search area (38 × 50 × 32 Å) using AutoDock Vina [57] as the docking software, with an exhaustiveness of 1,000. The identified docking sites were then reexamined using a smaller search area of (14 × 14 × 26 Å) for the tunnel and (14 × 20 × 26 Å) for the binding sites adjacent to Phe^{20}. The input for the docking calculations was prepared using AutoDockTools 4.2, [58] and figures were generated using the Python Molecule Viewer 1.5.6 software package [59].

2.9. $A\beta_{1-42}$ fibril formation

0.5 mL of 2 mM sodium hydride aqueous solution was added into the purchased $A\beta_{1-42}$ kit and treated with sonication at 0 °C for 30 min. 0.6 mL of 20 mM PBS was added to the sonicated solution, then incubated with an orbital shaker (300 rpm) at 37 °C for 72 h. The solution was diluted to experimental concentration with 10 mM PBS (pH = 7.4) before each experiment.

2.10. Fitting of $A\beta_{1-42}$ saturation titration analysis

$A\beta_{1-42}$, **BZ-OB**, and **NAP-OB** are virtually non-fluorescent, and a simplified formula can be used where the fluorescence intensity is directly proportional to the concentration of the $A\beta_{1-42}$–probe (**BZ-OB** or **NAP-OB**) complex only [60]:

$$I = \frac{1}{2}\mathrm{F} \times \left(([\mathrm{P}] + N[A\beta] + K_\mathrm{d}) - \sqrt{([\mathrm{P}] + N[A\beta] + K_\mathrm{d})^2 - 4N[A\beta][\mathrm{P}]} \right)$$

With F: a fluorescence proportionality factor, [P]: the initial concentration of **BZ-OB** or **NAP-OB**, [Aβ]: the initial concentration of $A\beta_{1-42}$, *N*: the number of equivalent binding sites on the Aβ fibril relative to Aβ monomer, and K_d: the dissociation constant. The results in Fig. 2E and F were obtained following a multi-parameter optimization of the experimental results following the fluorescence intensity at 642 or 621 nm, respectively, using a concentration of 1 or 0.5 μM $A\beta_{1-42}$ and total concentrations of **BZ-OB** or **NAP-OB** in PBS containing 1% DMSO. The slit width was set at 2.5/2.5. The best fittings were obtained for $N = 0.1$, i.e., one binding site per 10 $A\beta_{1-42}$, consistent with the hypothesized high affinity cross-β-sheet binding site on the protein fibril. Assuming different binding stoichiometries resulted in binding affinities within the same order of magnitude but increased uncertainty estimation ranges.

2.11. Preparation of AD mouse brain tissues

APP/PS1/TauP301L-BiFC triple transgenic mice presenting both amyloid and tau pathology were produced by the crossbreeding of APP/PS1 (APPswe/PSEN1E9 mice) with TauP301L-BiFC mice [61]. APP/PS1/TauP301L-BiFC triple transgenic mice were used in this study

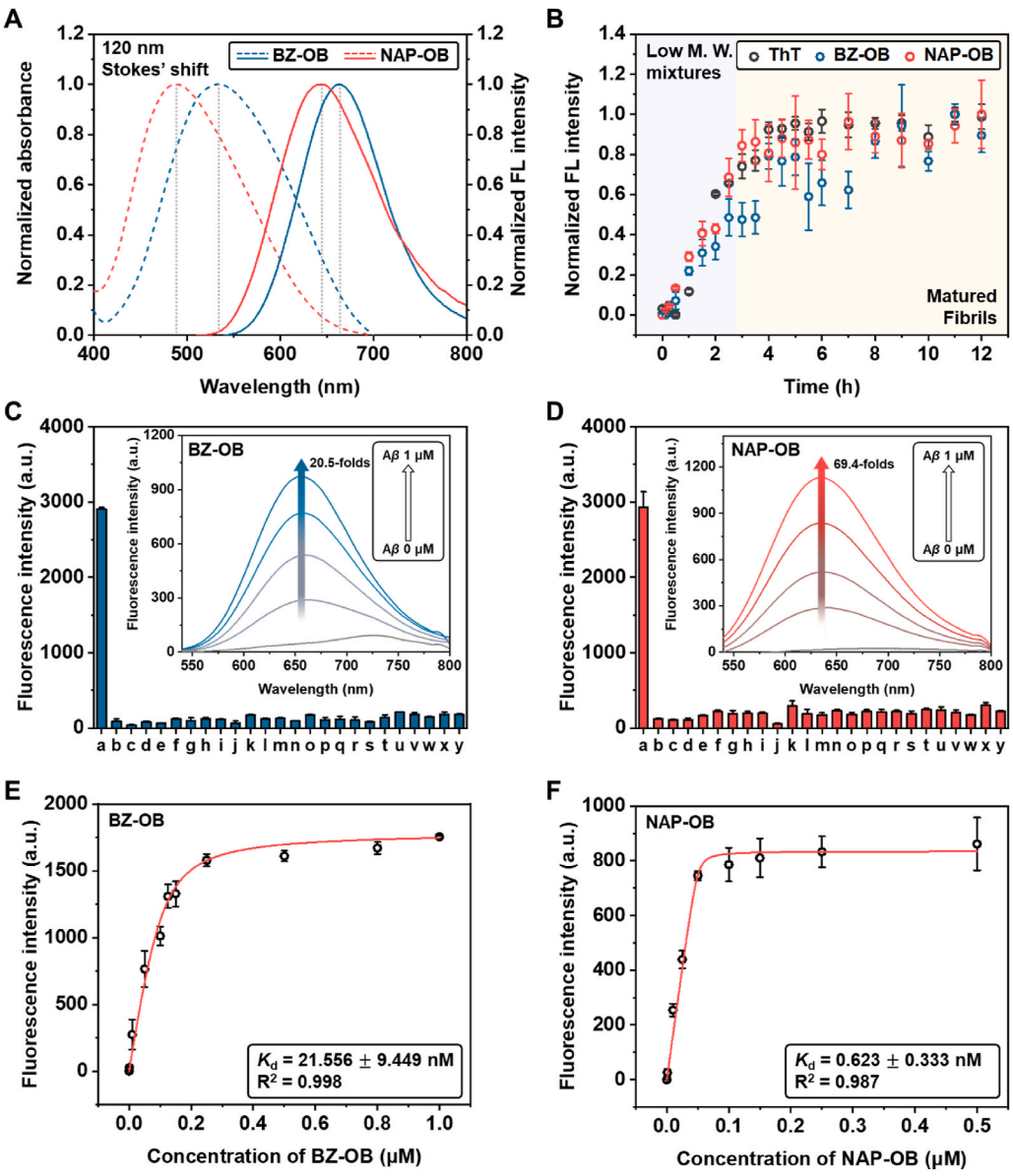

Fig. 2. Absorbance and fluorescence spectroscopy data of **BZ-OB** and **NAP-OB**. A) Absorption (dashed-line) and fluorescence (solid-line) spectra of **BZ-OB** (10 μM) and **NAP-OB** (10 μM) in the presence of $A\beta_{1\text{-}42}$ fibrils (10 μM), slit 2.5/2.5. B) Identification of $A\beta_{1\text{-}42}$ aggregation by Thioflavin T (ThT), **BZ-OB**, and **NAP-OB**. Selective fluorescence response assays for (C) **BZ-OB** and (D) **NAP-OB** with various potential interferents, a: $A\beta_{1\text{-}42}$ fibrils (10 μM); b–k: metal ions (1 mM, b: Mg^{2+}; c: Fe^{3+}; d: Fe^{2+}; e: Zn^{2+}; f: Ni^{2+}; g: K^{+}; h: Al^{3+}; i: Ca^{2+}; j: Cu^{2+}; k: Na^{+}); l–u: amino acids (1 mM, l: Glu; m: Phe; n: Tyr; o: Gly; p: Trp; q: Lys; r: Asn; s: His; t: Met; u: Val); v–y: thiols (1 mM, v: GSH; w: Hcy; x: DTT; y: Cys). Inset spectra indicate the change in the fluorescence intensity of (C) **BZ-OB** and (D) **NAP-OB** at 0, 0.25, 0.5, 0.75, and 1 μM of $A\beta_{1\text{-}42}$ aggregates. Saturation binding curves of (E) $A\beta_{1\text{-}42}$ fibrils (1 μM) as a function of **BZ-OB** (0–1 μM), and (F) $A\beta_{1\text{-}42}$ fibrils (0.5 μM) as a function of **NAP-OB** (0–0.5 μM) error ranges represent SD (n = 3), slit 5/5.

and the littermate APP/PS1, and wild-type mice were used as controls. For tissue preparation, mice were perfused with 0.9% saline and fixed with PBS containing 4% paraformaldehyde. Frozen brain samples embedded in O.C.T. were prepared at 30 μm thickness with a cryostat (Leica).

2.12. Fluorescent probe stain and image acquisition

To evaluate amyloid staining properties of **BZ-OB** and **NAP-OB**, 10 month-old of APP/PS1 and wild type brain tissue sections were stained with 10 μM of each fluorescent probe for 30 min and mounted onto glass glides. Fluorescence images were acquired using an Axio Scan Z1 (Zeiss) (**BZ-OB**: λ_{ex} = 540–546 nm and λ_{em} = 670–710 nm, **NAP-OB**: λ_{ex} = 540–546 nm and λ_{em} = 578–640 nm). To evaluate the amyloid staining property of **NAP-OB** in the presence of tau aggregation, brain tissue sections of 20 month-old of APP/PS1/TauP301L-BiFC brain tissue sections were stained with Sudan Black B solution (70% ethanol containing 0.05% Sudan Black B) for 10 min to reduce auto-fluorescence of aged brain tissue. Then the tissues were washed three times with PBS containing 0.1% Triton X-100 and washed with distilled water. For counterstaining nuclei, brain tissues were stained with Hoechst (0.5 μg/mL dissolved in distilled water) for 30 min. BiFC fluorescence (λ_{ex} = 460–490 nm and λ_{em} = 500–550 nm) images of whole brain tissues were acquired using Operetta (PerkinElmer) and Axio Scan Z1 (Zeiss). Then, the tissues were stained with **NAP-OB** (300 nM) for 30 min for staining amyloid plaques. Fluorescence images were acquired using an Axio Scan Z1 (Zeiss) (λ_{ex} = 540–546 nm and λ_{em} = 578–640 nm).

2.13. Image J analysis

The number and sizes of fluorescence-detected amyloid plaques were quantified by using the "analyze particle" tool of Image J (NIH) software. Fluorescence intensity profiles of amyloid plaques stained with each probe were generated by using the "interactive surface plots" tool of Image J (NIH) software. Signal to Noise ratio (S/N) was calculated from cortical area of three represent brain tissue images stained with each probe (Thioflavin S (ThS), **BZ-OB**, and **NAP-OB**).

3. Results and discussion

BZ-OB was synthesized *via* *o*-alkylation of deacetalized 2-(2,2-diethoxyethoxy)benzaldehyde with acetic acid followed by dehydration

of the resulting ether and **NAP-OB** was synthesized through a Bouveault aldehyde synthesis reaction from aryl 6-halide forms of naphthalene, followed by an aldol condensation reaction of the obtained 6-(dimethylamino)benzofuran-2-carbaldehyde (**BZ-CHO**) or 6-(dimethylamino)-2-naphthaldehyde (**NAP-CHO**) with 6-methyl heptane-2,4-dione as seen in Fig. 1 and Scheme S1. Fluorophores **BZ-OB** and **NAP-OB**, as is the case for the majority of currently described fluorescent dyes for Aβ, are D-π-A dyes and their significant Stokes' shifts, combined with a relatively broad featureless absorbance and emission spectra suggests they likely exhibit ICT behavior upon excitation. Therefore, these dyes' photophysical properties, particularly their ICT behavior, were investigated using several organic solvents (Table S2). The maximum wavelengths of absorption and emission of both fluorophores were measured concerning the solvent polarity, using the polarizability (induced dipole) and the dipolarity (permanent dipole) descriptions of solvent polarity, as reported in the Catalán data set [62]. The maximum absorption wavelength correlated well with the solvent polarizability, derived from the solvent-associated electronic stabilization of the Franck-Condon state. In contrast, the maximum fluorescence emission wavelength corresponded well with the solvent dipolarity, indicating that solvent cage rearrangement, following the geometrical relaxation of the excited states of **BZ-OB** and **NAP-OB** (Figs. S15 and S16), plays a major role. Collectively, these solvatochromic effects obviously support an excited state with a considerably higher dipole moment than the ground state, which is consistent with displaying ICT behavior in the excited state [63].

Additionally, the quantum yield of fluorescence is the highest in the most apolar solvents (~100%) and gradually decreases with the solvent polarity, with only 2.1 and 1.2% observed in methanol for **BZ-OB** and **NAP-OB**, respectively, which is a common observation in ICT-based fluorescent dyes [64,65]. Given the poor fluorescence quantum yield in aqueous media, the fluorophores could exhibit potentially considerable fluorescent turn-on ratios in the presence of the hydrophobic Aβ aggregates' interior. Importantly, to properly perform their function as an Aβ sensing probe and allow for potential *in vivo* experiments, these dyes need to maintain a reasonable solubility in aqueous media. The strategy of increasing hydrophobicity through π-elongation is a double-edged sword that can increase the binding affinity for hydrophobic analytes but simultaneously results in decreasing aqueous solubility, inducing aggregation-caused quenching (ACQ). As a maneuver to overcome an ACQ issue, an isobutyl moiety was introduced in both **BZ-OB** and **NAP-OB**, which prevented intermolecular aggregation through interference with crystal packing. The high aqueous solubility that followed from the introduction of this moiety was validated using concentration-dependent absorbance spectra. A linear relationship between concentration and absorbance was found at concentrations up to 50 μM for both **BZ-OB** and **NAP-OB** (Fig. S17), confirming the absence of aggregation in this concentration range, despite the relatively long π-conjugation of fluorophores **BZ-OB** and **NAP-OB**.

To support the existence of an ICT process in these dyes, the energy levels of their molecular orbitals in acetonitrile were calculated using DFT calculations (Fig. S18). The electron density distributions in the frontier orbitals unveiled an electron redistribution from the dimethylamino benzofuran or dimethylamino naphthalene moieties in the highest occupied orbital (HOMO) to the dioxaborine core in the lowest unoccupied orbital (LUMO). The involvement of an ICT process was further confirmed using TDDFT calculations, focusing on the degree of ICT based on the changes in electron density. Both fluorophores clearly exhibited a charge transfer upon excitation to the first excited state, which was dominated by the HOMO to LUMO transition, with a change in polarity upon excitation of 17.028 Debye and 14.598 Debye for **NAP-OB** and **BZ-OB**, respectively, resulting from a larger partial charge redistribution and larger distance between the donor and acceptor barycenters for **NAP-OB** (0.778e$^-$, 4.556 Å) as compared to **BZ-OB** (0.737e$^-$, 4.125 Å). These results correlate well with the observed stronger sensitivity of the Stokes' shift and maximum emission window to the polarity for **NAP-OB** (Fig. S16).

The absorbance and fluorescence emission spectra were determined in the presence of A$\beta_{1\text{-}42}$ fibrils. As can be seen from Fig. 2A, a maximum absorbance wavelength was observed at 523 nm and 495 nm for **BZ-OB** and **NAP-OB**, respectively, with a Stokes' shift of approximately 120 nm for both dyes, as the maximum emission bands were observed at 642 nm and 621 nm for **BZ-OB** and **NAP-OB**, respectively ($\lambda_{ex} = 523$ nm for **BZ-OB** and 495 nm for **NAP-OB**, Figs. 2A and S19). This fluorescence response emerges by two potential pathways: conformational restriction or polarity changes. As the fluorescence intensity hardly changed in function of increased viscosity in binary glycerol/ethylene glycol mixtures (Table S3 and Fig. S20), we assume that the fluorescence intensity mainly depends on microenvironmental polarity changes upon hydrophobic interactions with the β-sheet surface of A$\beta_{1\text{-}42}$ aggregate. Using the absorbance and fluorescence wavelengths of these dyes as a guide, the polarity of the environment sensed by these fluorophores matched best with diethyl ether for **BZ-OB** and tetrahydrofuran for **NAP-OB**, in accordance with previous reports on the polarity of the A$\beta_{1\text{-}42}$ aggregates' interior [43,60,66].

Next, a time-dependent coincubation with A$\beta_{1\text{-}42}$ pre-aggregates was carried out for **BZ-OB** and **NAP-OB**, as well as with the common Aβ aggregate fluorescent dye ThT, as a reference (Fig. 2B). As can be seen, the fluorescence intensity increased as the aggregate was formed, and **BZ-OB** and **NAP-OB** mimicked the fluorescent behavior of ThT, confirming their selectivity for the fibril forms of A$\beta_{1\text{-}42}$. The increased fluorescence of **BZ-OB** and **NAP-OB** was determined to be linearly dependent on the concentration of the A$\beta_{1\text{-}42}$ fibril, with a maximum of 20.5-fold and 69.4-fold fluorescence enhancement, respectively (inset of Fig. 2C and D). The fluorescent response of **BZ-OB** and **NAP-OB** to potential interferants, including metal ions, amino acids, and thiols, was negligible (Fig. 2C and D). The absorbance and fluorescence emission spectra were measured in the pH 2 to 12 range, and there was almost no change observed in the pH 4 to 10 range, while significant changes were observed at pH 2 or 12 (Fig. S23). Thus importantly, both fluorophores do not exhibit a pH dependence of the fluorescence under physiological pH conditions. **BZ-OB** and **NAP-OB** showed only a relatively weak fluorescence enhancement in the presence of BSA (Fig. S24), an essential consideration in polarity-dependent fluorescent probes for biomolecules, as albumin exhibits several hydrophobic sites and is a major carrier protein for hydrophobic drugs. In addition, a fluorescence titration of **BZ-OB** and **NAP-OB** with A$\beta_{1\text{-}42}$ fibrils revealed a binding affinity of $K_d = 21.56 \pm 9.45$ nM for **BZ-OB** and 0.62 ± 0.33 nM for **NAP-OB** (Fig. 2E and F). This value of **NAP-OB** represents a significantly higher affinity for A$\beta_{1\text{-}42}$ fibrils compared to the reported literature data for other dioxaborine-based curcumin structures (Table S1). To our best knowledge, this is the highest binding affinity as yet reported for all A$\beta_{1\text{-}42}$ fibril small-molecular fluorophores.

Additionally, the limit of detection (LOD) was found to be 13.071 and 10.813 nM for **BZ-OB** and **NAP-OB**, respectively (Fig. S25). This observation is somewhat surprising given the massive difference in K_d as well as a 3.4-fold higher fluorescence turn-on ratio for **NAP-OB**. However, a LOD of approximately 10 nM could be rationalized due to the relatively high instrument detection limit (IDL) of the fluorescence spectrometer caused by the turbidity induced by suspended Aβ aggregates, thus increasing the standard deviation of the blank.

A near-atomic-resolution cryo-EM structure of A$\beta_{1\text{-}42}$ was used as a protein scaffold for docking studies (Fig. 3A). As suggested before for other Aβ fluorophores, the hydrophobic tunnel architecture along the Aβ fibril axis, consisting of the residues of Phe^{19}, Asn^{27}, Gly^{29}, and Ile^{31}, could be the major binding site of **BZ-OB** and **NAP-OB** as cross-β-sheet binding ligands (Fig. 3B, D, and E for **BZ-OB** and 3C, F, and G for **NAP-OB**). However, the results of these theoretical studies need to be interpreted with some level of caution, as they do not provide a direct rationale for the observed binding affinity difference of **BZ-OB** and **NAP-OB**.

Next, we investigated whether probes **BZ-OB** and **NAP-OB** could

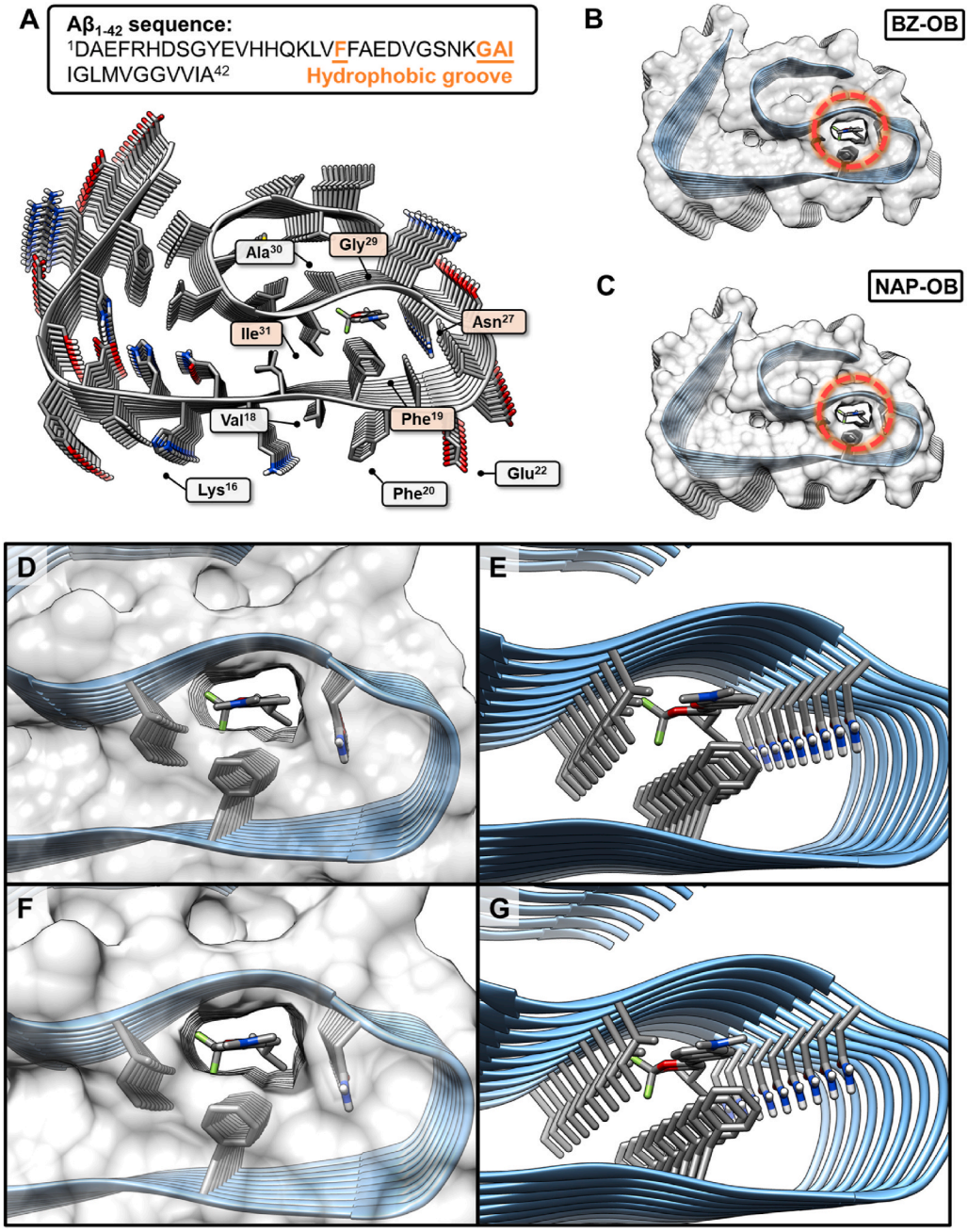

Fig. 3. Docking studies of the $A\beta_{1\text{-}42}$ protofibril (with a partial structure of the second protofibril). (A) $A\beta_{1\text{-}42}$ sequence and the location of key residues in the cryogenic electron microscopy (cryo-EM) (PBD: 5OQV) structure. Protein-ligand interactions in the internal tunnel (hydrophobic groove). Top view of (B) **BZ-OB** and (C) **NAP-OB**. (D) Zoomed top view, and E) clipped view of **BZ-OB**. (F) Zoomed top view and G) clipped view of **NAP-OB** encapsulated by the $A\beta_{1\text{-}42}$ Phe^{19}, Asn^{27}, Gly^{29}, and Ile^{31} surface within the tunnel.

potentially label amyloid plaques in biological tissue samples. Whole-brain tissue sections were prepared from 10 month-old APP/PS1 mice and littermate controls. Each brain tissue was incubated with 300 nM of **BZ-OB** and **NAP-OB** for 30 minutes. As anticipated, **BZ-OB** and **NAP-OB**-stained dot-shaped amyloid plaques in APP/PS1 brain tissue slices (Fig. 4A, S26–27). In contrast, no specific staining occurred in wild-type brain slices, in which Aβ is absent. High magnification images also showed a prominent staining ability for **NAP-OB** in detecting various sizes of amyloid plaques which co-localized well with ThS into compact and diffuse plaques (Fig. S28). An interactive surface plot analysis showed that **NAP-OB** has an outstanding S/N, which is comparable to that of ThS (**NAP-OB**: S/N = 3.5 ± 0.4, and ThS: S/N = 3.9 ± 0.6) (Fig. 4B). In comparison, **BZ-OB** was found not to stain small-sized plaques well, and its S/N was also lower than **NAP-OB** (**BZ-OB**: S/N = 1.8 ± 0.2). Quantification of the number and sizes of fluorescence-detected spots indicated that the amyloid labeling capacity of probe **NAP-OB** was comparable to that of ThS by presenting 68 ± 5 spots, with sizes below 100 μm^2 and 96 ± 11 spots, with sizes above 100 μm^2 (Fig. 4C). In comparison, **BZ-OB** detected a smaller number of amyloid plaques by showing only 12 ± 6 spots below 100 μm^2 and 43 ± 18 spots above 100 μm^2. Violin plots of spot areas indicated the distinguished staining pattern of **NAP-OB** comparable to that of ThS (Fig. 4D). These observations support **NAP-OB** as a reliable, red-colored amyloid tracer.

Next, we applied **NAP-OB** for staining amyloid plaques in the brain tissues of 20 month-old APP/PS1/TauP301L-BiFC mice, which present both Aβ plaques and fluorescently labeled tau aggregates [67]. Before the **NAP-OB** stain, Sudan Black B staining was performed to reduce autofluorescence of the aged mouse brain, and Tau-BiFC fluorescence was scanned by using a Zeiss Axio Scan (λ_{ex} = 460–490 nm and λ_{em} = 500–550 nm). Tau-BiFC fluorescence indicates tau aggregates ranging from oligomers to insoluble aggregates (Fig. 5A). Then, the tissues were stained with **NAP-OB** (300 nM) and scanned by using a Zeiss Axio Scan

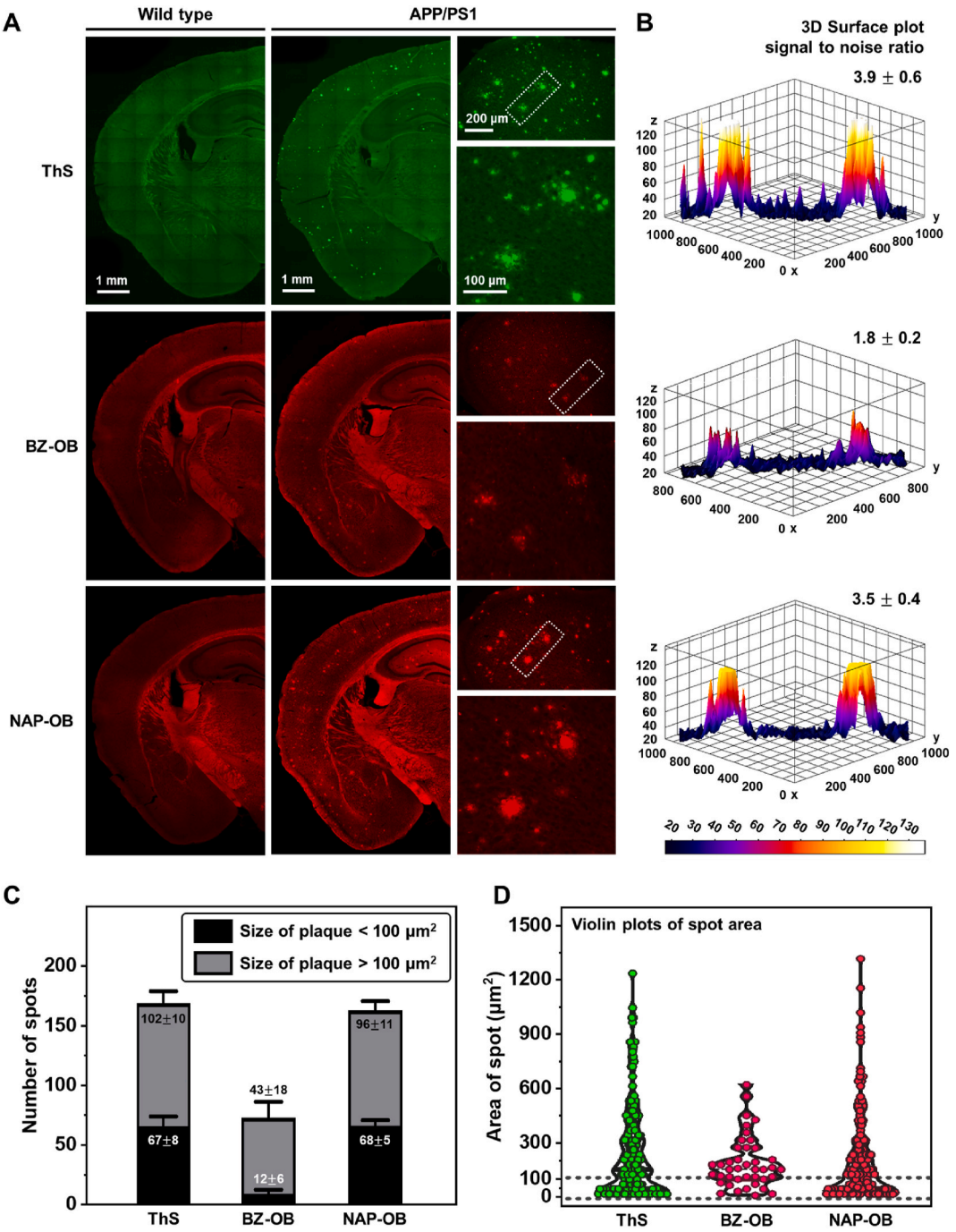

Fig. 4. Fluorescence images of wild type and APP/PS1 mouse brain tissues. (A) Fluorescence images of half brain tissue slices and magnified fluorescence images of motor cortices with Thioflavin S (ThS), **BZ-OB,** or **NAP-OB**. Scale bars indicate the length stated in the figure. (B) Interactive surface plots of the boxed area indicate the signal to noise ratio of ThS, **BZ-OB,** or **NAP-OB**. (C) Quantification of the number and sizes of fluorescence-stained amyloid plaque spots with ThS, **BZ-OB**, or **NAP-OB**. (D) Quantification of the Violin plots of spot areas to distinguish staining pattern of ThS, **BZ-OB**, or **NAP-OB**.

(λ_{ex} = 540–546 nm and λ_{em} = 578–640 nm). Spotanalysis indicated a total of 544 amyloid plaques stained with **NAP-OB** in half brain tissue of 20-month-old APP/PS1/Tau-BiFC mouse. Out of 544 plaques, 239 were tau-BiFC positive, indicating that tau proteins were co-aggregated with amyloid plaques in the brain. The median areas of tau negative and positive plaques were 51 μm^2 and 136 μm^2, respectively (Fig. 5B). This observation indicates that tau proteins are co-aggregated with large amyloid plaques, of which sizes are over 100 μm^2 rather than small ones. High magnification images of the subiculum show large amyloid plaques co-stained with tau-BiFC fluorescence (yellow arrows). In contrast, tau-BiFC fluorescence was not detected in most small amyloid plaques, below 100 μm^2 (Fig. 5C). These observations support that **NAP-OB**, unlike many other lipophilic pi-extended fluorescent probes, could reliably visualize senile plaques in the presence of other lipophilic protein aggregates, such as pTau tangles. In addition, its red-shifted fluorescence properties make these probes complementary with the green-fluorescent tau-BiFC system, while the emission windows of ThT and ThS overlap with BiFC and cannot be used. Thus, **NAP-OB** could find applications in differentiating aggregates, to study the co-occurrence of both protein aggregates in more detail, particularly so in the Tau-BiFC system.

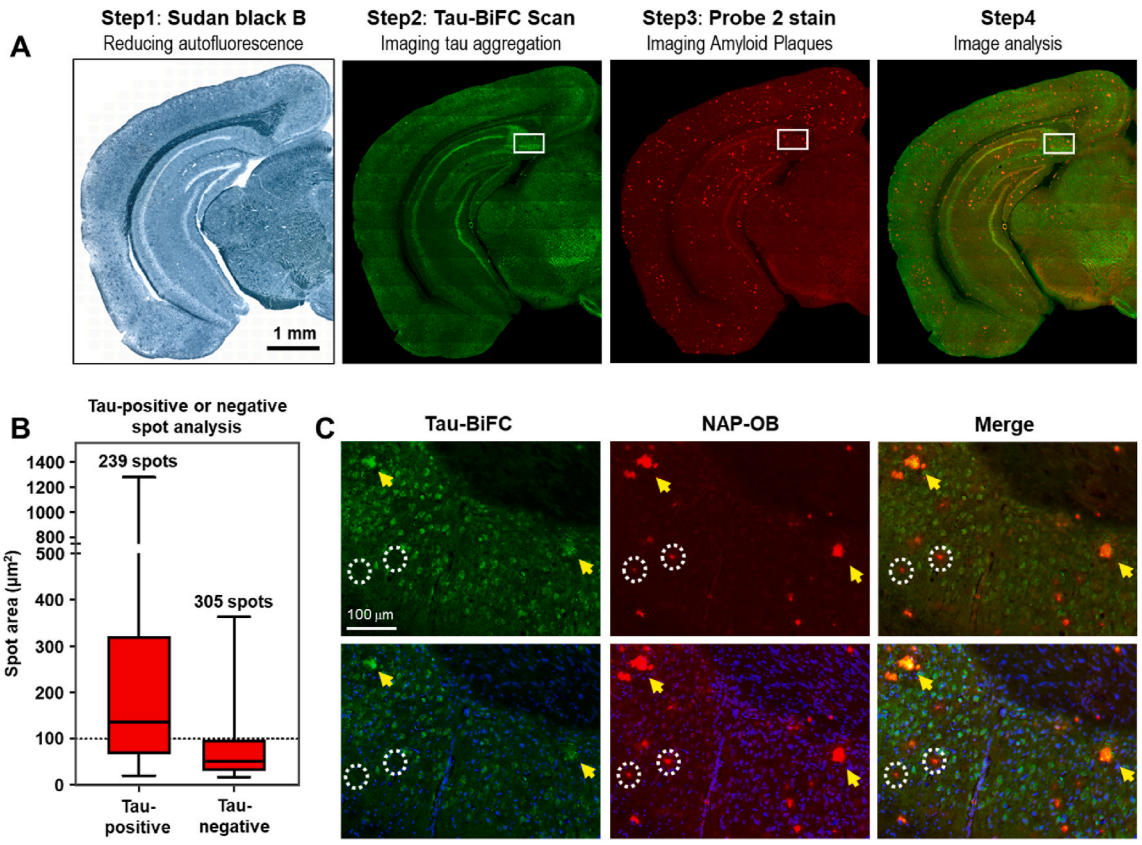

Fig. 5. Fluorescence images of the brain tissue slice of 20 month-old APP/PS1/TauP301L-BiFC mouse. (A) Staining protocol and the images; Step1: Sudan Black B stain, Step2: tau-BiFC fluorescence image acquisition. Step3; **NAP-OB** stain and fluorescence image acquisition, and Step4: image analysis. (B) Box and whisker plot analysis indicating the areas of amyloid plaques stained with **NAP-OB**. Out of 544 plaques detected in half brain tissue, 239 were tau-BiFC positive, and 305 plaques were tau-BiFC negative. (C) Magnified fluorescence images of the hippocampal subiculum. Yellow arrows indicate large plaques, which are co-stained with tau-BiFC and white circles indicate small plaques which are not stained with tau-BiFC. (For interpretation of the references to color in this figure legend, the reader is referred to the Web version of this article.)

4. Conclusions

In conclusion, two novel dioxaborine-based fluorescence dyes were designed and synthesized. In particular, the strategy of applying biannulated π-elongation to electron donor groups has successfully offered significantly lowered K_d values, i.e., higher binding affinity, for $A\beta_{1\text{-}42}$ fibrils. To the best of our knowledge, fluorophore **NAP-OB** exhibits the most potent affinity for $A\beta_{1\text{-}42}$ aggregates reported to date. The precise detection of Aβ species and knowledge about their emergence, accumulation, and evolution is indispensable for a detailed understanding of these neurodegenerative diseases, and the development of diagnostics and clinical intervention strategies, especially for early-stage disease. The structural modification presented here to enhance the sensitivity for Aβ may provide a rational path to the development of future small-molecule fluorophores. In terms of application, due to the efficient $^{18}F/^{19}F$ isotopic exchange at the central difluoro-boron complex structure, **NAP-OB** could find further applications as a dual fluorescence and PET imaging agent.

Funding

This research was supported by the National Research Foundation of Korea (CRI project no. 2018R1A3B1052702, NRF-2019M3E5D1A01068998, J. S. Kim), the Korea University Graduate School Junior Fellow Research Grant (J. An), the National Research Council of Science & Technology (NST) granted by the Ministry of Science, ICT & Future Planning (MSIP) (No. CRC-15-04-KIST), the Korea Health Technology R&D Project through the Korea Health Industry Development Institute (KHIDI) and Korea Dementia Research Center (KDRC), the Ministry of Health & Welfare and Ministry of Science and ICT, Republic of Korea (No. HI20C1234), and P. V. acknowledges support from Interne Fondsen KU Leuven/Internal Funds KU Leuven (STG/19/029).

CRediT authorship contribution statement

Jusung An: Project administration, Conceptualization, Data curation, Investigation, Software, Formal analysis, Writing – original draft. **Peter Verwilst:** Investigation, Data curation, Resources, Writing – review & editing, Funding acquisition. **Hira Aziz:** Data curation, Software, Formal analysis, Writing – original draft. **Jinwoo Shin:** Data curation, Software, Formal analysis. **Sungsu Lim:** Data curation, Formal analysis. **Ilwha Kim:** Methodology, Investigation. **Yun Kyung Kim:** Project administration, Conceptualization, Supervision, Funding acquisition, Writing – review & editing. **Jong Seung Kim:** Project administration, Conceptualization, Supervision, Funding acquisition, Writing – review & editing.

Appendix A. Supplementary data

Supplementary data to this article can be found online at https://doi.org/10.1016/j.bioactmat.2021.10.047.

References

[1] C.L. Masters, R. Bateman, K. Blennow, C.C. Rowe, R.A. Sperling, J.L. Cummings, Alzheimer's disease, Nat. Rev. Dis. Primers 1 (2015) 15056, https://doi.org/10.1038/nrdp.2015.56.

[2] J.M. Long, D.M. Holtzman, Alzheimer disease: an update on pathobiology and treatment strategies, Cell 172 (2019) 312–339, https://doi.org/10.1016/j.cell.2019.09.001.

[3] V.L. Villemagne, S. Burnham, P. Bourgeat, B. Brown, K.A. Ellis, O. Salvado, C. Szoeke, S.L. Macaulay, R. Martins, P. Maruff, D. Ames, C.C. Rowe, C.L. Masters, Amyloid β deposition, neurodegeneration, and cognitive decline in sporadic Alzheimer's disease: a prospective cohort study, the Lancet, Neurology 12 (2013) 357–367, https://doi.org/10.1016/S1474-4422(13)70044-9.

[4] G.S. Bloom, Amyloid-beta and tau: the trigger and bullet in Alzheimer disease pathogenesis, JAMA Neurol. 71 (2014) 505–508, https://doi.org/10.1001/jamaneurol.2013.5847.

[5] L.C. Serpell, Alzheimer's amyloid fibrils: structure and assembly, Biochim. Biophys. Acta 1502 (2000) 16–30, https://doi.org/10.1016/s0925-4439(00)00029-6.

[6] G.F. Chen, T.H. Xu, Y. Yan, Y.R. Zhou, Y. Jiang, K. Melcher, H.E. Xu, Amyloid beta: structure, biology and structure-based therapeutic development, Acta Pharmacol. Sin. 38 (2017) 1205–1235, https://doi.org/10.1038/aps.2017.28.

[7] S.A. Purro, M.A. Farrow, J. Linehan, T. Nazari, D.X. Thomas, Z. Chen, D. Mengel, T. Saito, T. Saido, P. Rudge, S. Brandner, D.M. Walsh, J. Collinge, Transmission of amyloid-beta protein pathology from cadaveric pituitary growth hormone, Nature 564 (2018) 415–419, https://doi.org/10.1038/s41586-018-0790-y.

[8] W.J. Young, S.W. Cho, J. Jung, Y. Huh, Y.S. Kim, D. Kim, K.H. Ahn, Frontiers in probing alzheimer's disease biomarkers with fluorescent small molecules, ACS Cent. Sci. 5 (2019) 209–217, https://doi.org/10.1021/acscentsci.8b00951.

[9] J. Rasmussen, H. Langerman, Alzheimer's disease - why we need early diagnosis, Degener. Neurol. Neuromuscul. Dis. 9 (2019) 123–130, https://doi.org/10.2147/DNND.S228939.

[10] F. Panza, M. Lozupone, G. Logroscino, B.P. Imbimbo, A critical appraisal of amyloid-beta-targeting therapies for Alzheimer disease, Nat. Rev. Neurol. 15 (2019) 73–88, https://doi.org/10.1038/s41582-018-0116-6.

[11] K. Pietrzak, K. Czarnecka, E. Mikiciuk-Olasik, P. Szymanski, New perspectives of alzheimer disease diagnosis – the most popular and future methods, Med. Chem. 14 (2018) 34–43, https://doi.org/10.2174/1573406413666171002120847.

[12] A. Zelmer, T.H. Ward, Noninvasive fluorescence imaging of small animals, J. Microsc. 252 (2013) 8–15, https://doi.org/10.1111/jmi.12063.

[13] J.V. Jun, D.M. Chenoweth, E.J. Petersson, Rational design of small molecule fluorescent probes for biological applications, Org. Biomol. Chem. 18 (2020) 5747–5763, https://doi.org/10.1039/D0OB01131B.

[14] P.L. Kastritis, J.P. Rodrigues, G.E. Folkers, R. Boelens, A.M. Bonvin, Proteins feel more than they see: fine-tuning of binding affinity by properties of the non-interacting surface, J. Mol. Biol. 426 (2014) 2632–2652, https://doi.org/10.1016/j.jmb.2014.04.017.

[15] S. Liu, D. Li, Z. Zhang, G.K.S. Prakash, P.S. Conti, Z. Li, Efficient synthesis of fluorescent-PET probes based on [^{18}F]BODIPY dye, Chem. Commun. 50 (2014) 7371–7373, https://doi.org/10.1039/C4CC01411A.

[16] J. Yang, R. Cheng, H. Fu, J. Yang, M. Kumar, J. Lu, Y. Xu, S.H. Liang, M. Cui, C. Ran, Half-curcumin analogues as PET imaging probes for amyloid beta species, Chem. Commun. 55 (2019) 3630–3633, https://doi.org/10.1039/c8cc10166c.

[17] P.C. Ke, M.A. Sani, F. Ding, A. Kakinen, I. Javed, F. Separovic, T.P. Davis, R. Mezzenga, Implications of peptide assemblies in amyloid diseases, Chem. Soc. Rev. 46 (2017) 6492–6531, https://doi.org/10.1039/C7CS00372B.

[18] P. Verwilst, H.S. Kim, S. Kim, C. Kang, J.S. Kim, Shedding light on tau protein aggregation: the progress in developing highly selective fluorophores, Chem. Soc. Rev. 47 (2018) 2249, https://doi.org/10.1039/c7cs00706j.

[19] E.D. Eanes, G.G. Glenner, X-ray diffraction studies on amyloid filaments, J. Histochem. Cytochem. 16 (1968) 673–677, https://doi.org/10.1177/16.11.673.

[20] M. Sunde, C.F. Blake, From the globular to the fibrous state: protein structure and structural conversion in amyloid formation, Q. Rev. Biophys. 31 (1998) 1–39, https://doi.org/10.1017/s0033583598003400.

[21] M.A. Findeis, The role of amyloid beta peptide 42 in Alzheimer's disease, Pharmacol. Ther. 116 (2007) 266–286, https://doi.org/10.1016/j.pharmthera.2007.06.006.

[22] S. Jin, N. Kedia, E. Illes-Toth, I. Haralampiev, S. Prisner, A. Herrmann, E. E. Wanker, J. Bieschke, Amyloid-beta(1-42) aggregation initiates its cellular uptake and cytotoxicity, J. Biol. Chem. 291 (2016) 19590–19606, https://doi.org/10.1074/jbc.M115.691840.

[23] H. Fu, M. Cui, P. Tu, Z. Pan, B. Liu, Evaluation of molecules based on the electron donor-acceptor architecture as near-infrared beta-amyloidal-targeting probes, Chem. Commun. 50 (2014) 11875–11878, https://doi.org/10.1039/C4CC04907A.

[24] J. Zhou, P. Jangili, S. Son, M.S. Ji, M. Won, J.S. Kim, Fluorescent diagnostic probes in neurodegenerative diseases, Adv. Mater. 32 (2020) 2001945, https://doi.org/10.1002/adma.202001945.

[25] E.E. Meyer, K.J. Rosenberg, J. Israelachvili, Recent progress in understanding hydrophobic interactions, Proc. Natl. Acad. Sci. U. S. A 103 (2006) 15739–15746, https://doi.org/10.1073/pnas.0606422103.

[26] H.J. Dyson, P.E. Wright, H.A. Scheraga, The role of hydrophobic interactions in initiation and propagation of protein folding, Proc. Natl. Acad. Sci. U. S. A 103 (2006) 13057–13061, https://doi.org/10.1073/pnas.0606422103.

[27] F. Xiao, Z. Chen, Z. Wei, L. Tian, Hydrophobic interaction: a promising driving force for the biomedical applications of nucleic acids, Adv. Sci. 7 (2020) 2001048, https://doi.org/10.1002/advs.202001048.

[28] M. Cui, M. Ono, H. Watanabe, H. Kimura, B. Liu, H. Saji, Smart near-infrared fluorescence probes with donor-acceptor structure for in vivo detection of beta-amyloid deposits, J. Am. Chem. Soc. 136 (2014) 3388–3394, https://doi.org/10.1021/ja4052922.

[29] Y.D. Park, J.H. Park, M.H. Hur, S.W. Kim, J.J. Min, S.H. Park, Y.J. Yoo, Y.J. Yoon, S.D. Yang, Fluorescent 2-styrylpyridazin-3(2H)-one derivatives as probes targeting amyloid-beta plaques in Alzheimer's disease, Bioorg. Med. Chem. Lett 22 (2012) 4106–4110, https://doi.org/10.1016/j.bmcl.2012.04.068.

[30] M. Ono, H. Watanabe, H. Kimura, H. Saji, BODIPY-based molecular probe for imaging of cerebral beta-amyloid plaques, ACS Chem. Neurosci. 3 (2012) 319–324, https://doi.org/10.1021/cn3000058.

[31] J. Yang, B. Zhu, W. Yin, Z. Han, C. Zheng, P. Wang, C. Ran, Differentiating Abeta40 and Abeta42 in amyloid plaques with a small molecule fluorescence probe, Chem. Sci. 11 (2020) 5238–5245, https://doi.org/10.1039/D0SC02060E.

[32] S.J. Jung, J.Y. Lee, T.H. Kim, D.E. Lee, J. Jeon, S.D. Yang, M.G. Hur, J.J. Min, Y. D. Park, Discovery of boronic acid-based fluorescent probes targeting amyloid-beta plaques in Alzheimer's disease, Bioorg. Med. Chem. Lett 26 (2016) 1784–1788, https://doi.org/10.1016/j.bmcl.2016.02.042.

[33] M. Xu, R. Li, X. Li, G. Lv, S. Li, A. Sun, Y. Zhou, T. Yi, NIR fluorescent probes with good water-solubility for detection of amyloid beta aggregates in Alzheimer's disease, J. Mater. Chem. B 7 (2019) 5535–5540, https://doi.org/10.1039/C9TB01012B.

[34] D. Kim, H. Moon, S.H. Baik, S. Singha, Y.W. Jun, T. Wang, K.H. Kim, B.S. Park, J. Jung, I. Mook-Jung, K.H. Ahn, Two-Photon absorbing dyes with minimal autofluorescence in tissue imaging: application to in vivo imaging of amyloid-beta plaques with a negligible background signal, J. Am. Chem. Soc. 137 (2015) 6781–6789, https://doi.org/10.1021/jacs.5b03548.

[35] K. Zhou, H. Fu, L. Feng, M. Cui, J. Dai, B. Liu, The synthesis and evaluation of near-infrared probes with barbituric acid acceptors for in vivo detection of amyloid plaques, Chem. Commun. 51 (2015) 11665–11668, https://doi.org/10.1039/c5cc03662c.

[36] M. Lee, M. Kim, A.F. Tikum, H.J. Lee, V. Thamilarasan, M.H. Lim, J. Kim, A near-infrared fluorescent probe for amyloid-β aggregates, Dyes Pigments 162 (2019) 97–103, https://doi.org/10.1016/j.dyepig.2018.10.013.

[37] X. Zhang, Y. Tian, C. Zhang, X. Tian, A.W. Ross, R.D. Moir, H. Sun, R.E. Tanzi, A. Moore, C. Ran, Near-infrared fluorescence molecular imaging of amyloid beta species and monitoring therapy in animal models of Alzheimer's disease, Proc. Natl. Acad. Sci. U. S. A 112 (2015) 9734–9739, https://doi.org/10.1073/pnas.1505420112.

[38] K. Ran, J. Yang, A.V. Nair, B. Zhu, C. Ran, CRANAD-28: a robust fluorescent compound for visualization of amyloid beta plaques, Molecules 25 (2020) 863, https://doi.org/10.3390/molecules25040863.

[39] Y. Li, J. Yang, H. Liu, J. Yang, L. Du, H. Feng, Y. Tian, J. Cao, C. Ran, Tuning the stereo-hindrance of a curcumin scaffold for the selective imaging of the soluble forms of amyloid beta species, Chem. Sci. 8 (2017) 7710–7717, https://doi.org/10.1039/C7SC02050C.

[40] J. Yang, F. Zeng, X. Li, C. Ran, Y. Xu, Y. Li, Highly specific detection of Abeta oligomers in early Alzheimer's disease by a near-infrared fluorescent probe with a "V-shaped" spatial conformation, Chem. Commun. 56 (2020) 583–586, https://doi.org/10.1039/C9CC08894F.

[41] C. Ran, X. Xu, S.B. Raymond, B.J. Ferrara, K. Neal, B.J. Bacskai, Z. Medarova, A. Moore, Design, synthesis, and testing of difluoroboron-derivatized curcumins as near-infrared probes for in vivo detection of amyloid-β deposits, J. Am. Chem. Soc. 131 (2009) 15257–15261, https://doi.org/10.1021/ja9047043.

[42] X. Zhang, Y. Tian, Z. Li, X. Tian, H. Sun, H. Liu, A. Moore, C. Ran, Design and synthesis of curcumin analogues for in vivo fluorescence imaging and inhibiting copper-induced cross-linking of amyloid beta species in Alzheimer's disease, J. Am. Chem. Soc. 135 (2013) 16397–16409, https://doi.org/10.1021/ja405239v.

[43] H. Fu, M. Cui, L. Zhao, P. Tu, K. Zhou, J. Dai, B. Liu, Highly sensitive near-infrared fluorophores for in vivo detection of amyloid-beta plaques in alzheimer's disease, J. Med. Chem. 58 (2015) 6972–6983, https://doi.org/10.1021/acs.jmedchem.5b00861.

[44] Y. Li, K. Wang, K. Zhou, W. Guo, B. Dai, Y. Liang, J. Dai, M. Cui, Novel D–A–D based near-infrared probes for the detection of β-amyloid and Tau fibrils in Alzheimer's disease, Chem. Commun. 54 (2018) 8717–8720, https://doi.org/10.1039/C8CC05259J.

[45] K.S. Park, M.K. Kim, Y. Seo, T. Ha, K. Yoo, S.J. Hyeon, Y.J. Hwang, J. Lee, H. Ryu, H. Choo, Y. Chong, A difluoroboron beta-diketonate probe shows "Turn-on" near-infrared fluorescence specific for tau fibrils, ACS Chem. Neurosci. 8 (2017) 2124–2131, https://doi.org/10.1021/acschemneuro.7b00224.

[46] J.M. Drake, M.L. Lesiecki, D.M. Camaioni, Photophysics and cis − trans isomerization of DCM, Chem. Phys. Lett. 113 (1985) 530–534, https://doi.org/10.1016/0009-2614(85)85026-0.

[47] A.M. Brouwer, Standards for photoluminescence quantum yield measurements in solution (IUPAC Technical Report), Pure Appl. Chem. 83 (2011) 2213–2228, https://doi.org/10.1351/PAC-REP-10-09-31.

[48] C. Xue, T.Y. Lin, D. Chang, Z. Guo, Thioflavin T as an amyloid dye: fibril quantification, optimal concentration and effect on aggregation, R. Soc. Open Sci. 4 (2017) 160696, https://doi.org/10.1098/rsos.160696.

[49] Gaussian 16, Revision C.01, M.J. Frisch, G.W. Trucks, H.B. Schlegel, G.E. Scuseria, M.A. Robb, J.R. Cheeseman, G. Scalmani, V. Barone, G.A. Petersson, H. Nakatsuji, X. Li, M. Caricato, A.V. Marenich, J. Bloino, B.G. Janesko, R. Gomperts, B. Mennucci, H.P. Hratchian, J.V. Ortiz, A.F. Izmaylov, J.L. Sonnenberg, D. Williams-Young, F. Ding, F. Lipparini, F. Egidi, J. Goings, B. Peng, A. Petrone, T. Henderson, D. Ranasinghe, V.G. Zakrzewski, J. Gao, N. Rega, G. Zheng, W. Liang, M. Hada, M. Ehara, K. Toyota, R. Fukuda, J. Hasegawa, M. Ishida,

T. Nakajima, Y. Honda, O. Kitao, H. Nakai, T. Vreven, K. Throssell, J. A. Montgomery Jr., J.E. Peralta, F. Ogliaro, M.J. Bearpark, J.J. Heyd, E. N. Brothers, K.N. Kudin, V.N. Staroverov, T.A. Keith, R. Kobayashi, J. Normand, K. Raghavachari, A.P. Rendell, J.C. Burant, S.S. Iyengar, J. Tomasi, M. Cossi, J. M. Millam, M. Klene, C. Adamo, R. Cammi, J.W. Ochterski, R.L. Martin, K. Morokuma, O. Farkas, J.B. Foresman, D.J. Fox, Gaussian, Inc., Wallingford CT, 2016.

[50] J.-D. Chai, M. Head-Gordon, Long-range corrected hybrid density functionals with damped atom-atom dispersion corrections, Phys. Chem. Chem. Phys. 10 (2008) 6615–6620, https://doi.org/10.1039/B810189B.

[51] V. Barone, P. Cimino, E. Stendardo, Development and validation of the B3LYP/N07D computational model for structural parameter and magnetic tensors of large free radicals, J. Chem. Theor. Comput. 4 (2008) 751–764, https://doi.org/10.1021/ct800034c.

[52] GaussView, , Version 6.1, R. Dennington, T.A. Keith, J.M. Millam, Semichem Inc., Shawnee Mission, KS, 2016.

[53] T.L. Bahers, C. Adamo, I. Ciofini, A qualitative index of spatial extent in charge-transfer excitations, J. Chem. Theor. Comput. 7 (2011) 2498–2506, https://doi.org/10.1021/ct200308m.

[54] T. Lu, F. Chen, Multiwfn: a multifunctional wavefunction analyzer, J. Comput. Chem. 33 (2012) 580–592, https://doi.org/10.1002/jcc.22885.

[55] T. Yanai, D.P. Tew, N.C. Handy, A new hybrid exchange-correlation functional using the Coulomb-attenuating method (CAM-B3LYP), Chem. Phys. Lett. 393 (2004) 51–57, https://doi.org/10.1016/j.cplett.2004.06.011.

[56] M. Kollmer, W. Close, L. Funk, J. Rasmussen, A. Bsoul, A. Schierhorn, M. Schmidt, C.J. Sigurdson, M. Jucker, M. Fandrich, Cryo-EM structure and polymorphism of Abeta amyloid fibrils purified from Alzheimer's brain tissue, Nat. Commun. 10 (2019) 4760, https://doi.org/10.1038/s41467-019-12683-8.

[57] O. Trott, A.J. Olson, AutoDock Vina, Improving the speed and accuracy of docking with a new scoring function, efficient optimization, and multithreading, J. Comput. Chem. 31 (2010) 455–461, https://doi.org/10.1002/jcc.21334.

[58] G.M. Morris, R. Huey, W. Lindstrom, M.F. Sanner, R.K. Belew, D.S. Goodsell, A. J. Olson, AutoDock4 and AutoDockTools4: automated docking with selective receptor flexibility, J. Comput. Chem. 30 (2009) 2785–2791, https://doi.org/10.1002/jcc.21256.

[59] M.F. Sanner, Python: a programming language for software integration and development, J. Mol. Graph. Model. 17 (1999) 57–61.

[60] J. Shin, P. Verwilst, H. Choi, S. Kang, J. Han, N.H. Kim, J.G. Choi, M.S. Oh, J. S. Hwang, D. Kim, I. Mook-Jung, J.S. Kim, Harnessing intramolecular rotation to enhance two-photon imaging of abeta plaques through minimizing background fluorescence, Angew. Chem. Int. Ed. 58 (2019) 5648–5652, https://doi.org/10.1002/anie.201900549.

[61] J.L. Jankowsky, H.H. Slunt, T. Ratovitski, N.A. Jenkins, N.G. Copeland, D. R. Borchelt, Co-expression of multiple transgenes in mouse CNS: a comparison of strategies, Biomol. Eng. 17 (2001) 157–165, https://doi.org/10.1016/S1389-0344(01)00067-3.

[62] J. Catalán, Toward a generalized treatment of the solvent effect based on four empirical scales: dipolarity (SdP, a new scale), polarizability (SP), acidity (SA), and basicity (SB) of the medium, J. Phys. Chem. B 113 (2009) 5951–5960, https://doi.org/10.1021/jp8095727.

[63] S. Grimme, J. Antony, S. Ehrlich, H. Krieg, A consistent and accurate ab initio parametrization of density functional dispersion correction (DFT-D) for the 94 elements H-Pu, J. Chem. Phys. 132 (2010) 154104, https://doi.org/10.1063/1.3382344.

[64] J. An, P. Jangili, S. Lim, Y.K. Kim, P. Verwilst, J.S. Kim, Multichromatic fluorescence towards aberrant proteinaceous aggregates utilizing benzimidazole-based ICT fluorophores, J. Inclusion Phenom. Macrocycl. Chem. 101 (2021) 205–215, https://doi.org/10.1007/s10847-021-01085-3.

[65] P. Verwilst, H.R. Kim, J. Seo, N.W. Sohn, S.Y. Cha, Y. Kim, S. Maeng, J.W. Shin, J. H. Kwak, C. Kang, J.S. Kim, Rational design of in vivo tau tangle-selective near-infrared fluorophores: expanding the BODIPY universe, J. Am. Chem. Soc. 139 (2017) 13393–13403, https://doi.org/10.1021/jacs.7b05878.

[66] C.H. Heo, K.H. Kim, H.J. Kim, S.H. Baik, H. Song, Y.S. Kim, J. Lee, I. Mook-jung, H. M. Kim, A two-photon fluorescent probe for amyloid β-plaques in living mice, Chem. Commun. 49 (2013) 1303–1305, https://doi.org/10.1039/C2CC38570H.

[67] S. Shin, D. Kim, J.Y. Song, H. Jeong, S.J. Hyeon, N.W. Kowall, H. Ryu, A.N. Pae, S. Lim, Y.K. Kim, Visualization of soluble tau oligomers in TauP301L-BiFC transgenic mice demonstrates the progression of tauopathy, Prog. Neurobiol. 187 (2020) 101782, https://doi.org/10.1016/j.pneurobio.2020.101782.